

Modeling plant composition as community continua in a forest landscape with LiDAR and hyperspectral remote sensing

C. R. HAKKENBERG,^{1,5} R. K. PEET,^{1,2} D. L. URBAN,³ AND C. SONG^{1,4}

¹Curriculum for the Environment and Ecology, University of North Carolina at Chapel Hill, Chapel Hill, North Carolina 27599 USA

²Department of Biology, University of North Carolina at Chapel Hill, Chapel Hill, North Carolina 27599 USA

³Nicholas School of the Environment, Duke University, Durham, North Carolina 27708 USA

⁴Department of Geography, University of North Carolina at Chapel Hill, Chapel Hill, North Carolina 27599 USA

Abstract. In light of the need to operationalize the mapping of forest composition at landscape scales, this study uses multi-scale nested vegetation sampling in conjunction with LiDAR-hyperspectral remotely sensed data from the G-LiHT airborne sensor to map vascular plant compositional turnover in a compositionally and structurally complex North Carolina Piedmont forest. Reflecting a shift in emphasis from remotely sensing individual crowns to detecting aggregate optical-structural properties of forest stands, predictive maps reflect the composition of entire vascular plant communities, inclusive of those species smaller than the resolution of the remotely sensed imagery, intertwined with proximate taxa, or otherwise obscured from optical sensors by dense upper canopies. Stand-scale vascular plant composition is modeled as community continua: where discrete community-unit classes at different compositional resolutions provide interpretable context for continuous gradient maps that depict n -dimensional compositional complexity as a single, consistent RGB color combination. In total, derived remotely sensed predictors explain 71%, 54%, and 48% of the variation in the first three components of vascular plant composition, respectively. Among all remotely sensed environmental gradients, topography derived from LiDAR ground returns, forest structure estimated from LiDAR all returns, and morphological-biochemical traits determined from hyperspectral imagery each significantly correspond to the three primary axes of floristic composition in the study site. Results confirm the complementarity of LiDAR and hyperspectral sensors for modeling the environmental gradients constraining landscape turnover in vascular plant composition and hold promise for predictive mapping applications spanning local land management to global ecosystem modeling.

Key words: community continua; gradient modeling; hyperspectral imaging; LiDAR; nonmetric multidimensional scaling; North Carolina Piedmont; predictive vegetation mapping; random forests; remote sensing; temperate forests; vascular plant composition.

INTRODUCTION

Efforts to model ecosystem functioning, map habitat quality, and monitor biodiversity in temperate forests hinge upon an accurate knowledge of the taxonomic composition of stands (Running and Coughlan 1988, Tilman et al. 1997). While field-based methods for mapping species composition can be highly accurate, they are extremely resource intensive at large spatial scales (Condit 1995). However, when paired with field plot data, aerial remote-sensing offers an efficient, repeatable, and synoptic platform by which to model forest properties at continuous, wall-to-wall extents (Schmidtlein et al. 2007, Anderson et al. 2008, Roth et al. 2015).

Remotely sensed imaging spectroscopy, or hyperspectral imaging, is one particularly powerful tool for mapping forest composition (Asner 1998, Clark et al. 2005).

Hyperspectral sensors are capable of distinguishing biochemical absorption features of biota at different narrow-band wavelengths that can be used to infer species-specific spectral signatures based on in-situ reflectance measurements and spectral libraries (Curran 1989). However, despite its potential, the direct estimation of leaf-level properties in complex canopies and at stand scales remains problematic. Several studies have noted how intra-specific variation in leaf optical properties can overwhelm attempts at species discrimination based on imaging spectroscopy alone (Price 1994, Ghiyammat and Shafri 2008). The ability to infer foliar chemistry from canopy reflectance, diagnostic of species-specific spectral signatures, is further complicated by factors including phenology, epiphyll cover, nonphotosynthetic vegetation, environmental conditions (including climate, nutrient availability, and biotic interactions), and, importantly, canopy structure (Okin et al. 2001). Indeed, elements of canopy structure, including height, stratification, plant architecture, and leaf orientation, shape the fundamental means by which photons interact with multiple surfaces in a forest canopy (Asner 1998). In structurally complex canopies, structural

Manuscript received 28 January 2017; revised 13 July 2017; accepted 13 September 2017. Corresponding Editor: Willem J. D. van Leeuwen.

⁵E-mail: chrisshakkenberg@gmail.com

elements can generate differential patterns in canopy shading that are capable of confounding attempts at inferring taxonomic identity from the reflectance properties of foliage alone (Torabzadeh et al. 2014).

To mitigate against these confounding effects while simultaneously distinguishing sub-canopy structural elements essential to an understanding of full-stand plant composition, active remote sensing instruments like LiDAR effectively complement passive (optical) instruments (Anderson et al. 2008, Higgins et al. 2014). And when combined, LiDAR-hyperspectral systems have been found to outperform either when used on its own (Hill and Thomson 2005, Leutner et al. 2012). In recent years, integrated LiDAR and hyperspectral imaging systems (hereafter referred to as "LiDAR-hyperspectral") have become increasingly prevalent, allowing for pixel-level fusion and calibration of both sensors in a single platform (Kampe et al. 2010, Cook et al. 2013).

In monospecific communities, or in open woodlands where individual tree crowns are spatially discrete, stand composition may be readily described by remotely identified upper-canopy crowns (Naidoo et al. 2012, Roth et al. 2015). However, in taxonomically and structurally complex forests, the characterization of vascular plant communities based on canopy dominants alone may be insufficient and potentially misleading when the majority of species are either smaller than the resolution of the remotely sensed imagery, intertwined with proximate taxa throughout the vertical strata of the forest, or otherwise obscured from overhead optical sensors by dense upper canopies (Thenkabail et al. 2004, Clark et al. 2005). Recognizing the infeasibility in identifying and tallying all sub-pixel and sub-canopy elements throughout complex forest stands, we instead shift the scale of focus to predict aggregate properties (and associated uncertainties) at the stand, rather than individual, level. It is, after all, at these larger stand scales, where the emergent properties of communities such as ecosystem processes, biodiversity, and habitat manifest (Ferrier and Guisan 2006, McGill et al. 2006). Modeling composition at a spatial resolution coarser than that of remotely sensed imagery likewise allows for a host of new derived predictors, such as those that rely on measures of sub-pixel heterogeneity to exploit the correlative relationship between aggregated remotely sensed predictors and the optical-structural properties of full stands (Ustin and Gamon 2010, Leutner et al. 2012).

Predominant approaches to modeling large-scale patterns in forest composition range from the depiction of forest communities as a patch mosaic of discrete polygons (Martin et al. 1998, Kokaly et al. 2003, Foster and Townsend 2004, Hill and Thomson 2005, Bunting et al. 2010, van Ewijk et al. 2014) to the portrayal of intergrading assemblages as continuous gradients overlaid on a pixel-based raster grid (Ohmann and Gregory 2002, Schmidtlein and Sassan 2004, Feilhauer and Schmidtlein 2009, Middleton et al. 2012, Gu et al. 2015, Neumann et al. 2015). This distinction in the representation of forest composition in geographic space has its historical

roots in the community-continua concept in community ecology. The community-continua concept reflects alternative, but complementary, approaches to the characterization of variation in species composition in space and time, that is defined simultaneously by the community-unit hypothesis, which describes ecological communities as distinct and repeatable entities (Daubenmire 1966), and the continuum theory, which envisions communities as idiosyncratic assemblages of overlapping yet independent species distributions (Whittaker 1967).

In this study, we employ a hybrid approach: using spatially nested field plot data in conjunction with airborne LiDAR-hyperspectral data to map vascular plant composition in a compositionally and structurally complex temperate forest as continuous ordination values, referenced by classified community units and remotely sensed environmental gradients. In so doing, we are guided by the following questions: How do community units compare with ordination gradients for partitioning vascular plant composition and modeling community turnover at landscape scales? What remotely sensible environmental gradients best describe compositional turnover in the study site, and how effective are LiDAR and hyperspectral sensors, when used in tandem, in explaining variation in floristic composition?

METHODS

Study site

The 2.8-km² study area consists of natural and semi-natural Piedmont forests located in the Blackwood Division of Duke Forest, Chapel Hill, North Carolina, USA. Following selective cutting, agriculture, and grazing in the 19th and early 20th centuries, the Blackwood Division largely transitioned to secondary old-field successional pine and mature hardwood forests (Peet and Christensen 1988). The precise boundaries of the study area are designed to capture core natural and semi-natural areas (excluding plantation forest, clear-cut, and built infrastructure) within the footprint of remotely sensed data (see *Methods: Remotely sensed data*). Duke Blackwood possesses modest topographic relief, with elevations ranging from 127 m to 228 m. Soils in the region exhibit a high degree of edaphic and hydrological variability, closely tracking substrate composition and topographic position, with sandy sediment-derived soils in floodplains and predominantly clay soils in the uplands (Stone et al. 1985). Temperatures in this section of the Piedmont range from a mean monthly minimum of 3.8°C in January to 31.1°C in July, with mean annual precipitation of 1,072 mm (Arguez et al. 2010).

Field data

Field plots were designed to span the spectrum of compositional variation and physiognomy throughout the study area to include upland, riparian, and bottomland

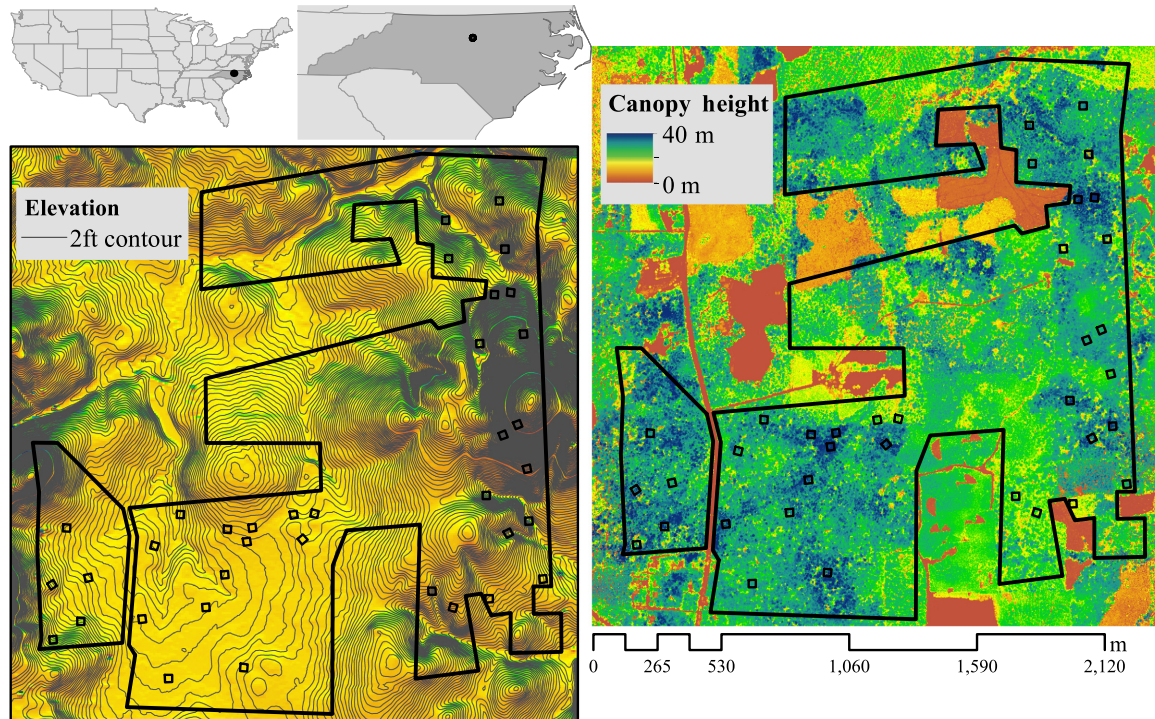


Fig. 1. Duke Forest Blackwood study area extent. The shape of the study area results from excluding areas of human habitation, plantation, and recently clear-cut forest. Canopy height (lower left) is derived from G-LiHT LiDAR and elevation (lower right) is depicted at 2 feet (0.6 m) contours, with open black squares representing plot location and extent.

forest stands. Our ad hoc definition of “stand-scale” is 900 m², a sampling extent with precedence in the North Carolina Piedmont (see Peet et al. 1998) that was deemed adequate for balancing the competing demands for a representative sample of plant composition, indicative of local stem size variance and cover density patterns, at the finest grain size possible (Appendix S1). Specific plot locations are based on a stratified random sampling design, randomly predetermined within the constraints of stratified bands along topographic gradients (Fig. 1; lower right). In all plots, cover values for all vascular plant species was recorded following Carolina Vegetation Survey protocols in 0.01-m², 0.1-m², 1-m², 10-m², and 100-m² spatially nested subplots, and in 400-m² and 900-m² full plots (Appendix S2). For woody stems reaching 1.4 m, species identity and diameter at breast height (DBH) was recorded for the entire 900-m² plot. While composition was ultimately assessed and modeled at 900 m², sampling of nested subplots at 0.01–100-m² scales allows for an efficient extrapolation of fine-scale composition to the full 900-m² scale (Peet et al. 1998). In total, 36 900-m² plots were sampled, together comprising 0.1% of the entire study area. Botanical nomenclature follows Weakley (2015), and the resultant plot data are available on Vegbank (*available online*, accession code: VB.pj.11067.DUKEBLACKWOODNA; Peet et al. 2012).⁶

Due to the importance of geo-locational precision in fitting field plots with relatively fine-resolution (2 × 2 m) remotely sensed imagery, all efforts were made to achieve sub-meter spatial locational accuracies for plot and sub-plot footprints. Because GPS signal interference in the dense forest canopy precluded the determination of sub-meter accuracies, plot and sub-plot locations were instead determined by measuring the distance of all plot vertices to three or more ground control points visible in 0.15-m resolution Digital Orthophoto Quadrangle (DOQ) imagery and in the field using tape measures (*available online*).⁷ By comparing field measurements with those from the DOQ in a GIS environment, we were able to triangulate plot vertex coordinates at sub-1-m accuracy.

Remotely sensed data

LiDAR and hyperspectral data covering the study area were collected with NASA Goddard’s LiDAR, Hyperspectral and Thermal (G-LiHT) airborne imager (Cook et al. 2013). G-LiHT consists of a scanning LiDAR, profiling LiDAR, imaging spectrometer, Global Positioning System and Inertial Navigation System (GPS-INS) and time server, data acquisition computer, and downwelling irradiance spectrometer. G-LiHT was designed to enable the integration of co-registered data

⁶<http://vegbank.org/cite/VB.pj.11067.DUKEBLACKWOODNA>

⁷<http://www.nconemap.com>

of similar grain size at the instrument level, rather than via post-hoc fusion of instrument data flown on different platforms and acquired on different dates. The system utilizes commercial, off-the-shelf instrumentation for use with local general aviation aircraft in an attempt to reduce costs and simplify worldwide deployment (Cook et al. 2013). The VQ-480 (Riegl USA, Orlando, Florida, USA) airborne laser scanning (ALS) system possesses a 60° field of view, a mean return density of up to 50 laser pulses/m², and a 10 cm diameter footprint at the nominal operating altitude of 335 m. The Hyperspec imaging spectrometer (Headwall Photonics, Fitchburg, Massachusetts, USA) operates in the 407–1,007 nm spectral region, providing 114 bands of imagery at a ≤5 nm full width half maximum spectral resolution and a 12-bit radiometric resolution. At a nominal flying altitude of 335 m and with a 50° field of view, the spectrometer provides imagery at a 2-m spatial resolution. Data for our study site were collected on 25 October 2013, during leaf-on conditions when inter-species phenological differences were accentuated.

All remotely sensed predictor variables were derived from four G-LiHT Level 3 raster products at a 2-m spatial resolution and a 2,982 × 1,988 pixel extent, including (1) a digital terrain model (DTM), (2) LiDAR returns, (3) a canopy height model (CHM), and (4) two 114-band atmospherically corrected hyperspectral surface reflectance image stacks taken before noon and after noon that day (Table 1). All derived LiDAR topography layers were calculated from the DTM at a 2-m resolution, with the exception of the topographic wetness index (TWI), which was also calculated at 4-m and 8-m resolutions to capture scale dependence in water-flow models (Beven and Kirkby 1979). LiDAR canopy height was derived from the canopy height model (CHM), while canopy and sub-canopy structural profiles were produced from the density and vertical distribution of all LiDAR returns. Hyperspectral imagery was converted to two classes of derived products. First, hyperspectral imagery was reduced to three Principal Components Axis (PCA) layers, accounting for 64%, 33.1%, 1.2% of variance among all bands respectively, and 98.3% cumulatively. In addition, narrow-band vegetation indices (VIs) with established precedence in the literature were employed as model predictors. These include carotenoid reflectance index 1 (CRI1), carotenoid reflectance index 2 (CRI2), photochemical reflectance index (PRI), red edge position index (REPI), simple ratio index (SRI), and normalized difference vegetation index (NDVI) (Table 1).

For modeling at a pixel resolution corresponding to the grain size of field plots, all derived geophysical variables at 2-m resolution (and 4-m and 8-m resolutions for TWI) were resampled at 30-m resolution based on summary statistics. Specifically, annualized solar radiation (ASR), deviation from mean elevation (DEV), elevation, slope, and topographic position index (TPI) were aggregated as the mean value of all 2-m pixels subsumed within the

greater 30-m pixels resolution. For CHM, the mean, minimum, maximum, standard deviation, skewness, and kurtosis was computed. All other variables were aggregated by mean, minimum, maximum, and standard deviation. Pixel aggregation reflects the dominant signal (i.e., mean), and sub-plot/sub-pixel variation (e.g., variance among 225 2-m sub-pixels is expressed by a single value in a 30-m aggregate pixel). All derived products and subsequent analyses were calculated using the software R, v. 3.3.1 (R Core Team 2016), with the exception of ASR, which was calculated using the ArcMap version 10.4 AASR plug-in (ESRI 2016).

Data analysis

Compositional ordination.—Ordination is an expedient tool for transforming large species-by-plot matrices into a reduced-dimensional space. This data reduction technique enables the relative abundance of species cover values in a plot to be referenced by its coordinates (mean and variance) in ordination space. In this study, ordination was performed using nonmetric multidimensional scaling (NMDS), a technique with precedence in the remote sensing and community ecology literature (Thessler et al. 2005). NMDS preserves the ordering relationship among samples in ordination space based on their ranked dissimilarity in compositional space (Legendre and Legendre 2012). Final scores are arbitrary in an absolute sense, but meaningful as relative indicators of n -dimensional compositional dissimilarity (where $n + 1$ represents the number of total species in a species-by-samples data matrix of relative abundances) in a more tractable k -dimensional ordination space (where $k < n - 1$). NMDS was chosen over alternative ordination methods because it makes no assumptions about dimensionality, linearity, nor the shape of species-response curves to gradients (Kruskal 1964). Because the NMDS procedure seeks to align sample data according to ecological dissimilarity in ordination space, we first derived a compositional distance matrix among plots using Bray-Curtis dissimilarity, a distance matrix for species data that controls for bias due to joint absences and double weights joint presence as a strong indicator of resemblance (Legendre and Legendre 2012). Before running NMDS, rare species occurring on <5% of plots were removed from the data set (Appendix S3).

To determine the optimum number of ordination axes, a step-down procedure was performed to determine goodness-of-fit based on 180 preliminary NMDS runs (30 runs each on one to six dimensions). With extension to higher dimensions only producing marginal improvements in goodness of fit, the three-axis solution was deemed an acceptable solution balancing model parsimony (low dimensionality) and explanatory power. Combined, NMDS 1–3 explained 76% of all variation in vascular plant composition ($R^2 = 0.76$; Appendix S4). Because the numerical NMDS algorithm cannot guarantee a global solution, the model was run for 2,000 iterations and the

TABLE 1. LiDAR and hyperspectral remote sensing predictor variables†.

Category and predictor	Abbreviation	Equation/Source
LiDAR topography (last returns)		
Average solar radiance (annual)	ASR	ESRI (2016)
Deviation from mean elevation	DEV	$DEV = (z_0 - \bar{z})/SD$; where z_0 is the elevation of the focal pixel, \bar{z} and SD are mean and standard deviation of elevation in a 222-m window (De Reu et al. 2013)
Height above EGM96 (Earth Gravitational Model 1996) geoid	elev	DTM (Cook et al. 2013)
Slope in degrees	slope	DTM (Cook et al. 2013)
Topographic position index	TPI	$TPI = z_0 - \bar{z}$; where z_0 is the elevation of the focal pixel and \bar{z} is mean elevation in a 222 m window (De Reu et al. 2013)
Topographic wetness index	TWI	$TWI = \ln(a/\tan\beta)$; where a is the local upslope area and β is slope (Beven and Kirkby 1979)
LiDAR canopy structure (first/all returns)		
All return heights	all returns	LiDAR returns (Cook et al. 2013)
Canopy height model	CHM	CHM (Cook et al. 2013)
Returns per pulse	RPP	LiDAR returns (Cook et al. 2013)
Tree return heights‡	tree returns	LiDAR returns (Cook et al. 2013)
Understory return heights‡	understory returns	LiDAR returns (Cook et al. 2013)
Hyperspectral foliar reflectance§		
Anthocyanin reflectance index 1	ARI1	$ARI1 = \frac{1}{\rho_{550}} - \frac{1}{\rho_{700}}$ (Gitelson et al. 2001)
Anthocyanin reflectance index 2	ARI2	$ARI2 = \rho_{800} \left[\frac{1}{\rho_{550}} - \frac{1}{\rho_{700}} \right]$ (Gitelson et al. 2001)
Carotenoid reflectance index 1	CRI1	$CRI1 = \frac{1}{\rho_{510}} - \frac{1}{\rho_{550}}$ (Gitelson et al. 2002)
Carotenoid reflectance index 2	CRI2	$CRI2 = \frac{1}{\rho_{510}} - \frac{1}{\rho_{700}}$ (Gitelson et al. 2002)
Normalized difference vegetation index (narrowband)	NDVI	$NDVI = \frac{\rho_{800} - \rho_{670}}{\rho_{800} + \rho_{670}}$ (Haboudane et al. 2004)
Principal component axes 1–3	PCA1–3	full spectrum PCA axis 1–3 ($\rho_{407} : \rho_{1007}$)
Red edge position index	REPI	$\max[(\rho_n + 1 - \rho_n)/10]$ where $690 \leq n \leq 750$ (Haboudane et al. 2004)
Simple ratio index (narrowband)	SRI	$SRI = \rho_{800}/\rho_{670}$ (Haboudane et al. 2004)

†All 2×2 m remotely sensed predictors aggregated at a 30×30 m (900 m^2) output resolution.

‡Tree vs. understory returns defined as all returns above and below 1.37 m, respectively.

§ ρ_n ; where n is wavelength in nm.

solution with the lowest dissimilarity between ordination and Bray-Curtis distances was selected as the final model. As there is no intrinsic ordering to the final NMS ordination axes, axis scores were rotated using PCA to align them along orthogonal axes of maximum floristic variation. All procedures in the NMDS analysis, including the derivation of dissimilarity matrices, were performed using the ecodist package (Goslee and Urban 2007) in R, v. 3.3.1 (R Core Team 2016).

Community-unit classification.—Parsimonious partitionings of field plot compositional data were determined using the optimal partitioning of similarity relations (optpart) unsupervised classification function (Roberts 2016b). Optpart is a non-hierarchical, iterative reallocation algorithm that seeks to maximize the partana ratio, a measure of similarity comparing within-cluster vs. among-cluster Bray-Curtis index scores for a given number of clusters (Aho et al. 2008). Optpart has been found to consistently rank among the highest performing clustering algorithms based on goodness-of-clustering evaluators across data sets and dissimilarity matrices (Aho et al. 2008, Roberts 2015). Because no one a priori

number of classes exists that optimizes the trade-offs between sensitivity and specificity for a given data set, we first evaluated relative performance in class differentiability from two to eight clusters, with two clusters being the minimum number of possible clusters, and more than eight groupings deemed excessively large for so small an area (Kaufman and Rousseeuw 2005). Among the seven cluster combinations, the two- and seven-cluster solutions were ultimately adopted for community-unit classification as both possess locally maximum partana ratios and mean silhouette widths, the mean similarity of each plot to other plots in its cluster vs. its similarity to the most similar cluster (Appendix S5). Following community-unit clustering, community labels and diagnostic species were apportioned to all clusters to reference the central taxonomic concept and physiognomy of each community type. Diagnostic species were likewise assessed for each community unit based on indicator species scores and canopy dominance. Indicator species (the product of the relative frequency and relative average abundance in clusters) were determined using the indval function in labdsv package in R (Roberts 2016a), while canopy

dominance is based on cover when present (Chytrý et al. 2002).

Compositional modeling.—Candidate algorithms with precedence for the predictive modeling of forest composition with remotely sensed data include random forests (Leutner et al. 2012, Naidoo et al. 2012), support vector regression (e.g., Middleton et al. 2012), nearest neighbor approaches (Ohmann and Gregory 2002, Thessler et al. 2005), and partial least squares regression (Feilhauer et al. 2011, Neumann et al. 2015). In this study, random forests (RF) was ultimately selected as the algorithm best able to maximize predictive accuracy and generalizability (Appendix S6), while simultaneously balancing concerns regarding limited training data, high data dimensionality, and collinearity among predictors (Evans et al. 2011). RF is a nonparametric modeling approach well-suited to high-dimensional, “small n large p ” (where p is the number of features) ecological data, variables exhibit nonlinear and complex interactions (Pal 2005). The RF algorithm utilizes an ensemble of classification trees to produce highly accurate and unbiased predictions based on votes across bootstrap replicates that are largely immune to over-fitting (Prasad et al. 2006). For reference classifications, field plot groupings corresponding to each of the designated community units were used to train a RF classification model parameterized with all remotely sensed predictors (Table 1) over 2000 separate trees using the randomForest package in R (Liaw and Wiener 2002). Continuous gradient modeling, on the other hand, was performed by running three parallel RF regression models, each parameterized with remotely sensed predictors and trained to field data, to predict continuous values for NMDS axes 1–3 across the study site.

While the RF algorithm is robust to multi-collinearity and over-fitting, prediction accuracy can be affected when the number of features (p) is significantly higher than the number of samples (n ; Tološi and Lengauer 2011). Thus, for each of the three predictive models, feature selection was performed to optimize accuracy and generalizability by reducing the total number of parameters. To accomplish this, full models utilizing all predictors were run for each of the three continuous response variables (i.e., NMDS 1–3) and predictive accuracy was recorded based on 10-fold cross-validation, an out-of-bag (OOB) model evaluation procedure that iteratively withholds random subsamples of the training data for use as a quasi-independent validation of model fit. Thereafter, features were iteratively withheld, until convergence on a final set of predictors that maximizes cross-validated prediction accuracy (Appendix S7). Feature-selected models, trained with all field plot data and remotely sensed inputs, were then used to predict NMDS axis scores for all pixels throughout the study area. Predicted values are based on the majority or mean vote for regression and classification, respectively, while uncertainties are derived from the standard deviation of

all OOB observations. All predicted values were rescaled to the range of NMDS values in the training data set (Zhang and Lu 2012). As a visual aid, predicted NMDS 1–3 scores were scaled to an eight-bit dynamic range and displayed in red-green-blue (RGB) using a modal filter for noise reduction and visual clarity (Appendix S8).

Predictive accuracy estimates are based on 1,000 permutations of 10-fold cross-validated estimates, each with random splits of training and test data to produce per-pixel posterior distributions of mean accuracy (R^2) and variance (SD; Kohavi 1995). Because significance in the statistical relationship between remotely sensed predictors and NMDS axes 1–3 is obscured in the black box RF model, post-hoc Spearman correlations, a rank-based measure of association that facilitates application to non-normal data distributions, were run for all predictors (Prasad et al. 2006, Evans et al. 2011). The final Spearman correlation matrix and environmental biplots include all remaining predictors after feature selection in RF regression models.

RESULTS

In total, 208 vascular plant taxa were identified in sampled field plots, among which 144 species remained after removing rare species occurring on less than 5% of all plots (Appendix S3). Vascular plant species richness ranged from 35 to 100 species per plot (mean = 61 species). Species' cover was relatively evenly distributed (mean Pielou's evenness $J = 0.73$), with all field plots containing 5–20 species with over 10% cover (Appendix S9). In addition to relatively high taxonomic diversity, field plots exhibited a relatively large degree of structural heterogeneity, with woody stems exhibiting a broad size distribution, from the minimum recorded 0.1-cm DBH to 101.5 cm DBH (mean DBH = 7.6 cm; DBH standard deviation = 11.7 cm). Within field plots, *Acer rubrum*, *Liquidambar styraciflua*, *Liriodendron tulipifera*, *Quercus alba*, and *Pinus taeda* possessed the highest cover values (in descending order) and *Acer rubrum*, *Carya glabra*, *Cornus florida*, *Muscadinia rotundifolia*, *Nyssa sylvatica*, *Prunus serotina*, and *Toxicodendron radicans* occurred on all plots.

Based on locally maximum partana ratios and mean silhouette widths, the two- and seven-cluster solutions were adopted as the most compositionally distinct and parsimonious classification of field plots into community units (Appendix S5). Units are labeled to reference the physiognomy of each community type (e.g., upland sub-xeric vs. bottomland hydric) as well as its central taxonomic concept by means of diagnostic species (Table 2). Nonmetric multidimensional scaling (NMDS) ordinated biplots demonstrate relative compositional similarity among field plots and classified community units that reduce n -dimensional compositional space to three principal component axes of NMDS space, and finally to a single semantically meaningful RGB color referencing the location of plot coordinates and

TABLE 2. Community-unit classification.

Label	Diagnostic species
Two class	
Upland sub-xeric (USX)	<i>Quercus montana</i> , <i>Juniperus virginiana</i> , <i>Amelanchier arborea</i> , <i>Vaccinium pallidum</i>
Mixed mesic (MM)	<i>Liriodendron tulipifera</i> , <i>Ulmus alata</i> , <i>Polystichum acrostichoides</i> , <i>Euonymus americanus</i> , <i>Aesculus sylvatica</i>
Seven class	
Upland sub-xeric (USX)	<i>Quercus montana</i> , <i>Juniperus virginiana</i> , <i>Amelanchier arborea</i> , <i>Vaccinium pallidum</i>
Midslope sub-xeric (MSX)	<i>Carya pallida</i> , <i>Oxydendrum arboreum</i> , <i>Smilax bona-nox</i> , <i>Chimaphila maculata</i>
Midslope mesic (MSM)	<i>Liriodendron tulipifera</i> , <i>Carya tomentosa</i> , <i>Hylodesmum nudiflorum</i> , <i>Uvularia perfoliata</i>
Pine mixed (PM)	<i>Pinus taeda</i> , <i>Liquidambar styraciflua</i> , <i>Muscadinia rotundifolia</i> , <i>Vaccinium pallidum</i>
Riparian (R)	<i>Carpinus caroliniana</i> , <i>Aesculus sylvatica</i> , <i>Polystichum acrostichoides</i> , <i>Galium tinctorium</i>
Toe-slope mesic (TM)	<i>Quercus falcata</i> , <i>Carya ovata</i> , <i>Rubus pensilvanicus</i> , <i>Arisaema triphyllum</i>
Bottomland hydric (BH)	<i>Quercus michauxii</i> , <i>Carpinus caroliniana</i> , <i>Smilax rotundifolia</i> , <i>Carex flaccosperma</i>

community-unit volumes in ordination space (Fig. 2). The nested relationship between the two- and seven-community-unit classifications in ordination space is reflected in geographic space as a more intricate partitioning of the mapped study area at the finer, seven-unit compositional resolution (Fig. 3a, b). Predictive models of continuous ordination scores, on the other hand, are intended to best reflect realistic landscape patterning among intergrading stand assemblages. Based on 1,000 permutations of the 10-fold cross-validation accuracy assessment procedure, RF predictive models account for 71%, 54%, and 48% of the variance in NMDS axes 1–3,

respectively (Table 3). Community-unit classified maps (Fig. 3a, b), as well as subsequent community legends, reference discrete community types in the gradient map and provide ecological context to the otherwise artificial ordination scores (Fig. 3e).

For the parallel goal of interpreting primary ordination axes in relation to remotely sensible environmental gradients, we assessed the relationship between featured-selected LiDAR-hyperspectral predictors and field plot ordination scores. Spearman coefficients indicate that topographic variables like elevation and TWI load highly onto NMDS 1, measures of canopy structure

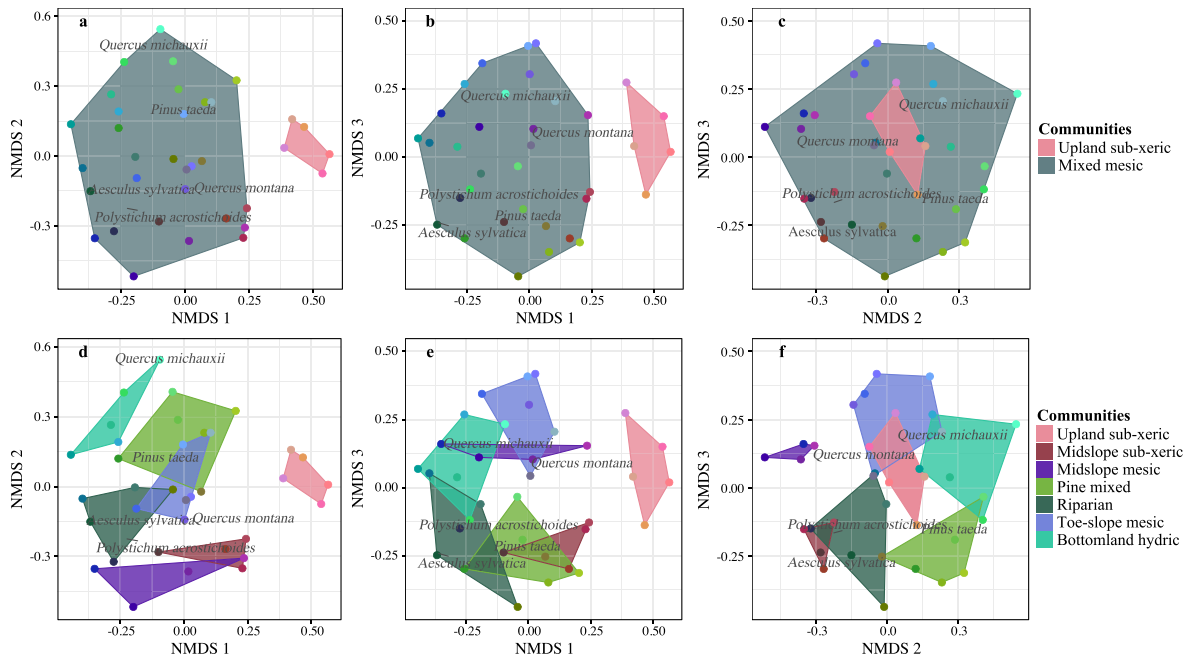


Fig. 2. Field plots are represented in three two-dimensional slices of three-dimensional NMDS space, and classified into (a–c) two and (d–f) seven community-unit clusters. Chart colors represent the three-dimensional NMDS coordinates of field plots (points) and community units (convex hulls) as RGB color combinations, with NMDS1 scores mapped along the red spectrum, NMDS2 as green, and NMDS 3 as blue. Unlike field plot points, community-unit convex hulls represent each class’s central concept and group centroid in NDMS space. The location of selected diagnostic species (dark gray) reference their weighted average in NDMS space.

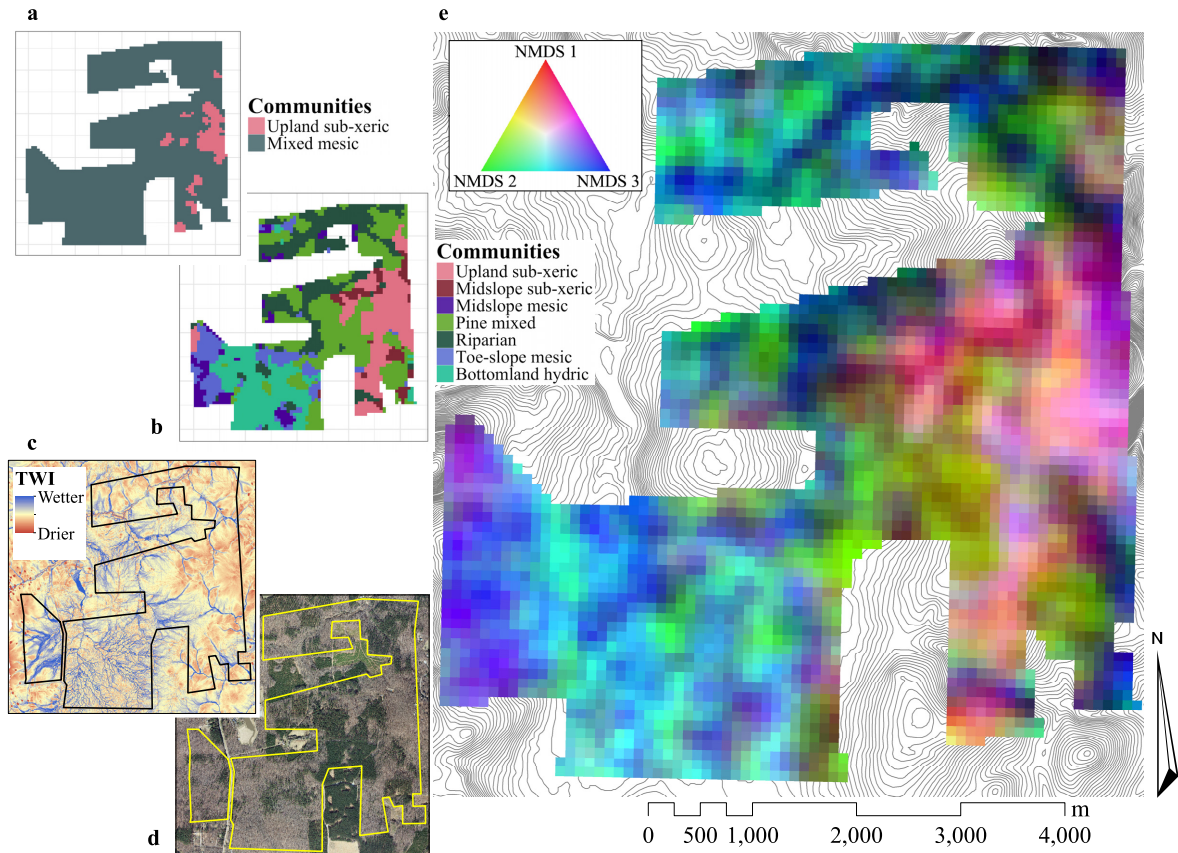


FIG. 3. Predictive maps of vascular plant community continua. (a) Two-community-unit classification; (b) seven-community-unit classification; (c) topographic wetness index (TWI); (d) fine resolution leaf-off DOQ imagery (<http://www.nconemap.com>); (e) continuous gradient map of ordinated NMDS axes 1–3, with each axis mapped onto red, green, and blue color guns, respectively. Colors are consistent with Fig. 2 in that they reference the predicted compositional identity of each pixel as a function of its three-dimensional location in NMDS ordination space.

TABLE 3. RF regression model and parameters (post feature selection).

NMDS axis	CV R^2 †	CV R^2 SD†	Feature selected predictor variables‡
1	0.71	0.02	elev (mean), PCA1 (mean)
2	0.54	0.03	CHM (SD), all returns (skew), PCA2 (maximum), CRI1 (SD), PCA1 (minimum), TWI (8 m minimum), tree returns (SD)
3	0.48	0.04	REPI (mean), RPP (minimum), CRI2 (mean)

†Mean and standard deviation (SD) CV R^2 of 1,000 permutations of the 10-fold cross-validation procedure.

‡See Table 1 for abbreviations.

(e.g., standard deviation of the canopy height model and skewness of all returns) are significantly correlated with compositional variation along NMDS 2, and narrow-band VIs like REPI and CRI2, as well as LiDAR return density (RPP), distinguish between broadleaf and conifer canopies along the NMDS 3 axis (Table 4). Viewed as three two-dimensional slices of three-dimensional NMDS space, correlation vectors, representing variables across the three primary RS data domains of LiDAR topography, LiDAR canopy structure, and hyperspectral reflectance, appear to occupy all sectors of the compositional ordination space (Fig. 4).

DISCUSSION

Community units in compositional space

Envisioned as a discrete entity, community units are nominal categories that express a significant degree of cohesion between stands (or field plots) in relation to alternative groupings (Peet and Roberts 2013, Roberts 2015). Viewed in ordination space, the two-class partitioning of field plots reveals a highly distinct and spatially discrete set of five points whose compositional identity, as evidenced by the correspondence between

TABLE 4. Spearman correlation matrix: RS predictors vs. NMDS 1–3 ordination scores.

RS data domain and predictor†	NMDS 1	NMDS 2	NMDS 3
LiDAR topography (last returns)			
elev (mean)	0.761	–	–
TWI (8 m minimum)	–0.505	0.428	0.409
LiDAR canopy structure (first/all returns)			
All returns (skew)	–0.368	–0.526	–
Tree returns (SD)	–	–0.495	–
CHM (SD)	–	–0.628	–
RPP (minimum)	–	–	0.428
Hyperspectral foliar reflectance			
PCA1 (mean)	0.536	0.345	–
PCA1 (minimum)	0.45	0.491	–
PCA2 (maximum)	0.491	–	–
CRI1 (SD)	–	–0.362	–
CRI2 (mean)	0.488	–	–0.34
REPI (mean)	–	–	0.605

Note: Cells with a dash indicate non-significant ordinations, where $P > 0.05$.

†See Table 1 for abbreviations.

plot point color and that of the convex hull, closely matches that of the central concept of the upland sub-xeric community unit (Fig. 2a–c). By contrast, the disparity between the multi-colored points and the muddled gray of the generically labeled mixed mesic class confirms visually what its relatively low mean silhouette width (0.13 vs. 0.40 for upland sub-xeric) otherwise indicates: the mixed mesic class is perhaps too generic (and the two-class solution too coarse) for effective ecological characterization. Expanding the field plot partitioning from two to seven classes reveals a hierarchically nested topology of field plots, whereby supervised classification of the mixed mesic community unit results in it being split into six component parts, leaving the upland sub-

xeric class undisturbed. Compared to the two-unit classification, the composition of field plots in the seven-class schema possesses higher fidelity to the central concept of each of their respective community units, a conclusion visually illustrated by the color correspondence between plot points and community convex hulls (Fig. 2d–f).

Community-unit maps confirm that the distinct aggregation of the two-class solution in ordination space is mirrored in geographical space, as the location of the outlying upland sub-xeric class is constrained to the higher elevation areas on the east side of the study area (Fig. 3a). Compared with the two-class map, the seven-unit classification reveals a more reticulated pattern of interlocking patches that track known cover types and physiognomic contours of the landscape (Fig. 3b). For example, visual observation confirms that the botanically defined bottomland hydric category corresponds with the fine-scale dendritic venation characteristic of topographically defined bottomlands visible in the same location in classified and gradient maps (Fig. 3c). While compositionally similar to the flat bottomlands, steep stream channels constrain the distribution of botanically defined riparian communities to the north. Pine mixed communities form an “H” shape in the center of the study area, as verified in leaf-off reference imagery (Fig. 3d).

Gradient mapping of compositional continua

The recognition that community assemblages are fundamentally continuous in space and dynamic through time, coupled with the need for the realistic characterization of landscape gradients in composition, has given rise to the predictive mapping of continuous ordination scores (Schmidtlein et al. 2007, Feilhauer et al. 2011, Middleton et al. 2012). Given a representative group of field plots whose location in ordination space exhibits a statistically significant relationship with remotely sensed environmental and reflectance data, predictive models can be effectively employed to interpolate the mean and variance of new samples or pixels (Gu et al. 2015, Singh

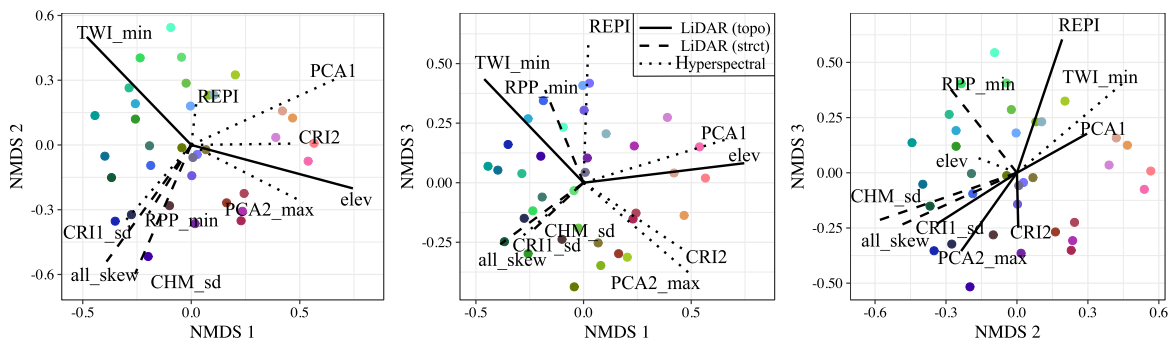


FIG. 4. NMDS 1–3 environmental biplots. Field plot points in all three two-dimensional ordination spaces reflect their three-dimensional NMDS coordinates as a unique RGB color combination. Vectors represent statistically significant ($p \neq 0$; $P < 0.05$) remotely sensed predictors of NMDS axes 1–3 from the three RS data domains: LiDAR topography (topo; solid line), LiDAR canopy structure (strct; dashed line), and hyperspectral reflectance (dotted line). The direction and magnitude of each vector is proportional to the Spearman coefficient of correlation with each respective NMDS axis. Predictors are defined in Table 1.

et al. 2015). As an abstraction of n -dimensional compositional space reduced to k axes, predicted ordination scores (along with their subsequent estimates of variance) reference a distinct volume in ordination space whose specific location is meaningful in relation to the composition of sampled field plots.

Derived remotely sensed predictors accounted for between 48% and 71% of the variance in vascular plant composition, reflecting both the impediments and potential in predicting vascular plant composition from LiDAR-hyperspectral data. These accuracies are within the range of those found in other studies predicting the composition of canopy vegetation. For example, Schmidlein and Sassin (2004) modeled the first two NMDS axes of a Bavarian grassland with an accuracy (R^2) of 0.71 and 0.66, respectively. Gu et al. (2015) predicted forest composition in Wisconsin, USA with an accuracy of 0.67 and 0.47 for NMDS 1 and 2, respectively. While caution is advised against the direct comparison of predictive accuracies among studies employing disparate methodologies, that accuracies for predicting full stand composition (including undetected understory flora) match those from studies restricted to directly detected upper canopy biota, reaffirms the potential for the full-stand, predictive modeling approach.

Remotely sensed environmental gradients constrain compositional space

Nonparametric data mining approaches have been praised for their ability to exploit nonlinear, non-intuitive relationships to drive highly accurate model predictions (Prasad et al. 2006). However, as black-box correlative models, they are limited in the extent to which they can uncover the role of individual parameters in guiding model predictions (Evans et al. 2011). If they are explanatory, it is because they are sufficiently accurate and generalizable (Houlahan et al. 2016). Thus for the parallel, but ultimately separate, task of inferring the environmental gradients driving predictive models of composition, we assessed the significance, sign, and magnitude of the relationship between individual remotely sensed predictors and ordinated compositional axes.

LiDAR-derived terrain variables like elevation and TWI were significantly correlated with NMDS axis 1, confirming the predominant role of topography as an indirect driver of forest composition along this first primary component of compositional variation (Table 4). Clearly visible elevation gradients and stream channels in the NMDS 1 predictive map confirms this interpretation (Fig. 3; Appendix S10). These findings reflect the view that vegetation patterns in the Piedmont's rolling topography largely track catenal formations, characterized by sandy, nutrient-poor soils in the uplands and moist, nutrient-rich soils of the bottomland shrink-swell clays and the more silty, periodically submerged, riparian areas (Stone et al. 1985). Despite these edaphic and hydrologic differences, riparian and bottomland communities share some

common characteristics, both possessing significant overlap in species composition and tending toward higher stem density and species richness values compared to their upland counterparts (Matthews et al. 2011).

Indicators of forest structure derived from LiDAR first and all returns were among the strongest individual predictors of variance along NMDS 2 (Table 4). Among them, the standard deviation of the canopy height model (CHM), which provides a metric of canopy height variation as well as the presence of gaps, and the skewness of all LiDAR returns, which indicates the degree to which biomass is concentrated in the lower vs. the upper canopy, possessed the largest correlation with NMDS 2 (Kane et al. 2010). In both cases, compositional turnover along the NMDS 2 axis largely adheres to a gradient in canopy structural heterogeneity, such that increasing NMDS 2 values suggest increasingly homogeneous canopy structures. This spatial turnover in structural complexity largely reflects a successional gradient in the study area, such that more taxonomically complex, late successional communities are characterized by increased frequency in canopy gaps as well as larger variation in crown size and shape (Peet and Christensen 1988, Canham et al. 1994). Interestingly, CR11 (SD), a proxy for variance in carotenoid pigments in a 30-m window, is likewise significantly correlated with NMDS 2, partly resulting from the correlation between spectral and structural heterogeneity ($\rho = 0.34$; $P < 0.05$) in complex, multi-cohort stands (Rocchini et al. 2015).

Hyperspectral VIs were particularly informative for detecting a leaf type and crown habit gradient in canopy cover across the spectrum of NMDS 3: from pure conifer, through mixed forests, to primarily hardwood forests (Appendix S10c). Narrowband VIs effectively discriminate trends in aggregate canopy pigmentation, including chlorophyll and carotenoids, accentuated in the study area due to partial leaf senescence in the October image date (Gitelson et al. 2002, Haboudane et al. 2004). NMDS 3 was negatively correlated with the red-edge position index (REPI), a narrow-band VI particularly adept at the detection of greenness gradients due to differential leaf chlorophyll content and water stress (Filella and Penuelas 1994). The negative relationship indicates that, with changing fall colors, greenness decreases with increasing proportion of broadleaf foliage. This relationship between remotely sensed greenness indices and large-scale compositional variation has been observed in other studies and reflects the capacity of aggregated foliar biochemical traits as a diagnostic tool for assessing forest composition (Naidoo et al. 2012, Gu et al. 2015). Concurrently, NMDS 3 is positively correlated with the carotenoid reflectance index 2 (CRI2), indicating a greater proportion of orange-red carotenoid pigments in broadleaf forests undergoing partial leaf senescence (Gitelson et al. 2002). LiDAR return density (RPP) complements hyperspectral VIs by discriminating the degree of upper canopy perviousness to incoming LiDAR pulses (Kane et al. 2010). In this case, RPP

effectively distinguishes between the homogenous canopy structure of secondary pine stands and the more heterogeneous mixed hardwood classes (Anderson et al. 2008, Higgins et al. 2014).

Despite some degree of collinearity between the hyperspectral and LiDAR data domains, the two were nonetheless able to explain a substantial proportion of variance across all sectors of the ordination space (Fig. 4). To date, there remains a lack of consensus regarding the added value of LiDAR data in addition to hyperspectral imagery for modeling forest composition, especially for space-borne sensors at medium-resolutions like AVIRIS (Leutner et al. 2012, Gu et al. 2015). However, at smaller spatial scales, we find that LiDAR-derived variables, especially those like height variance in LiDAR returns that exploit the sensor's high precision, are significant (and, in fact, prominent) in detecting the primary remotely sensible environmental gradients driving compositional variation (Hill and Thomson 2005, Higgins et al. 2014).

Ecological applications and implications

The characterization of spatial turnover in composition as a patch mosaic of community units vs. a continuous gradient of ordination scores has important implications for the utilization and interpretation of compositional maps (Austin 2013, Hakkenberg et al. 2017). Classified maps of spatially discrete community patches are an expedient simplification of compositional complexity and idiosyncrasy that can be of great utility for describing coarse land cover types (e.g., Gergely and McKerrow 2016), as well as hierarchical vegetation classifications (Jennings et al. 2009, Peet and Roberts 2013). However, they can be problematic for rigorous ecological applications. First, because no single unambiguous solution may exist in the unsupervised classification procedure, the determination of the number of classes to be employed in supervised classification can be somewhat arbitrary, and ultimately dependent upon expert opinion (Aho et al. 2008, Roberts 2016b). For example, despite the relative merits of the two- and seven-unit solutions in this study, each possesses conspicuous drawbacks (Appendix S9). While parsimonious, the two-unit classification is too generic a solution to adequately reflect the range of compositional dissimilarity among field plots. Concurrently, the more finely resolved seven-unit solution errs in distinguishing too many closely related compositional types and suffers from low overall classification accuracy owing to overlap and confusion when pixels are erroneously classified to adjacent community types (Appendix S11). With so many classes, the seven-unit grouping likewise suffers from low per-unit sample sizes, insufficient for a statistically rigorous accuracy assessment (Congalton 1991).

But more fundamentally, mapped community units are themselves conceptually problematic when the discreteness of their boundaries obscures consideration of

what is ultimately a continuous phenomenon. At their heart, community units are expedient simplifications of n -dimensional species assemblages that exist simultaneously as a conceptual category and a geographic entity (Austin 2013). As an abstract category defined by numerical analysis of representative field plots into resolved community types, community units serve as the fundamental building blocks of a hierarchically organized vegetation classification system (Chytrý et al. 2002, Jennings et al. 2009, Peet and Roberts 2013). However, when rendered in geographic space, the imposition of discrete boundaries to what is otherwise continuous turnover in composition may impart undesired artefacts to compositional maps and subsequent applications (Cushman et al. 2010). Gradient maps, on the other hand, circumvent the downsides of discrete categorization and readily lend themselves to modeling applications where the depiction of realistic landscape vegetation patterning is paramount, such as predictive habitat modeling and functional trait mapping (Gu et al. 2015, Neumann et al. 2015, Singh et al. 2015). However, as abstractions of compositional space, they fail to convey a readily communicated interpretation of the ecological and environmental patterns underlying it (Evans and Cushman 2009).

Ultimately, the relative strengths and weaknesses of community and continuum approaches invite synthesis. In this study, we modeled stand-scale turnover in vascular plant composition as continuous gradients referenced by discrete community units, both as geographic entities (maps) and as conceptual categories (map legends). By depicting composition in terms of RGB color combinations, n -dimensional compositional complexity can be effectively reduced to a single, visually interpretable symbol that is semantically meaningful as an indicator of its volume (and centroid) in three-dimensional ordination space. Provided consistency in color mapping and an ancillary legend, community units provide vital context and guide navigation of the otherwise abstract ordination scores.

CONCLUSION

With evidence accumulating for the role of local and global environmental change in altering ecological processes in forest ecosystems, efforts to monitor forest composition from remote platforms will likely increase rapidly in the years to come. This study demonstrates an example of the community-continua concept in the predictive mapping of vascular plant composition, interpretable as turnover in ecological units as well as remotely sensed environmental gradients. Results confirm the complementarity of three remotely sensed environmental data domains, topography from LiDAR ground returns, forest structure from LiDAR all returns, and foliar traits from hyperspectral imagery, to explain variance along the three primary axes of floristic composition in the study site. But in light of these results, future

research is needed to better assess the transferability of remote sensing approaches to the predictive modeling of vegetation in different settings and across spatial scales. Of particular interest is the utility of LiDAR-hyperspectral systems in extending static niche models to actively incorporate the temporal dynamics of disturbance and biotic competition. With the deployment of a fleet of new LiDAR and hyperspectral air- and spaceborne sensors, the monitoring of temporal turnover in composition will be increasingly feasible, providing a wealth of new data for inference into pattern and process in the spatiotemporal dynamics of vascular plant composition.

ACKNOWLEDGMENTS

This work was supported under the NASA Earth and Space Science Fellowship Program Grant NNX14AK92H and the Center for the Study of the American South. Technical assistance was provided by Peter S. White, Michael Lee, Sam Tessel, and Bianca Lopez. In addition, we thank Bruce D. Cook for provision of G-LiHT data, the Duke Forest field office, as well as field assistants: Jeffery Berger, Joshua Bradley, Per Frisk, Alec Keiper, Nicole Murnighan, Matthew Seibert, and Stephanie Trillo-ordonez. Finally, we would also like to thank two anonymous reviewers who provided excellent feedback in revising this article.

LITERATURE CITED

- Aho, K., D. Roberts, and T. Weaver. 2008. Using geometric and non-geometric internal evaluators to compare eight vegetation classification methods. *Journal of Vegetation Science* 19:549–562.
- Anderson, J. E., L. C. Plourde, M. E. Martin, B. H. Braswell, M. L. Smith, R. O. Dubayah, M. A. Hofton, and J. B. Blair. 2008. Integrating waveform lidar with hyperspectral imagery for inventory of a northern temperate forest. *Remote Sensing of Environment* 112:1856–1870.
- Arguez, A., Durre, I., Applequist, S., Squires, M., Vose, R., Yin, X. and Bilotta, R. 2010. NOAA's U.S. Climate Normals (1981–2010). NOAA National Centers for Environmental Information, National Centers for Environmental Information, NESDIS, NOAA, U.S. Department of Commerce.
- Asner, G. P. 1998. Biophysical and biochemical sources of variability in canopy reflectance. *Remote Sensing of Environment* 64:234.
- Austin, M. P. 2013. Vegetation and environment: discontinuities and continuities. Pages 71–106 in J. Franklin and E. van der Maarel, editors. *Vegetation ecology*. John Wiley and Sons, Chichester, West Sussex, UK.
- Beven, K. J., and M. J. Kirkby. 1979. A physically based, variable contributing area model of basin hydrology. *Hydrological Sciences Journal* 24:43–69.
- Bunting, P., R. M. Lucas, K. Jones, and A. R. Bean. 2010. Characterisation and mapping of forest communities by clustering individual tree crowns. *Remote Sensing of Environment* 114:2536–2547.
- Canham, C. D., A. C. Finzi, S. W. Pacala, and D. H. Burbank. 1994. Causes and consequences of resource heterogeneity in forests: interspecific variation in light transmission by canopy trees. *Canadian Journal of Forest Research* 24:337–349.
- Chytrý, M., L. Tichý, J. Holt, and Z. Botta-Dukát. 2002. Determination of diagnostic species with statistical fidelity measures. *Journal of Vegetation Science* 13:79–90.
- Clark, M. L., D. A. Roberts, and D. B. Clark. 2005. Hyperspectral discrimination of tropical rain forest tree species at leaf to crown scales. *Remote Sensing of Environment* 96:375–398.
- Condit, R. 1995. Research in large, long-term tropical forest plots. *Trends in Ecology and Evolution* 10:18–22.
- Congalton, R. G. 1991. A review of assessing the accuracy of classifications of remotely sensed data. *Remote Sensing of Environment* 37:35–46.
- Cook, B. D., L. A. Corp, R. F. Nelson, E. M. Middleton, D. C. Morton, J. T. McCorkel, J. G. Masek, K. J. Ranson, V. Ly, and P. M. Montesano. 2013. NASA Goddard's LiDAR, hyperspectral and thermal (G-LiHT) airborne imager. *Remote Sensing* 5:4045–4066.
- Curran, P. J. 1989. Remote sensing of foliar chemistry. *Remote Sensing of Environment* 30:271–278.
- Cushman, S., J. Evans, K. McGarigal, and J. Kiesecker. 2010. Toward Gleasonian landscape ecology: from communities to species, from patches to pixels. United States Department of Agriculture, Forest Service Rocky Mountain Research Station, Fort Collins, Colorado, USA.
- Daubenmire, R. 1966. Vegetation: identification of typical communities. *Science* 151:291–298.
- De Reu, J., et al. 2013. Application of the topographic position index to heterogeneous landscapes. *Geomorphology* 186:39–49.
- ESRI. 2016. ArcGIS Desktop: Release 10.4. ESRI, Redlands, California, USA.
- Evans, J. S., and S. A. Cushman. 2009. Gradient modeling of conifer species using random forests. *Landscape Ecology* 24:673–683.
- Evans, J. S., M. A. Murphy, Z. A. Holden, and S. A. Cushman. 2011. Modeling species distribution and change using random forest. Pages 139–159 in C. Drew, Y. Wiersma, and F. Huettmann, editors. *Predictive species and habitat modeling in landscape ecology*. Springer, New York, New York, USA.
- Feilhauer, H., and S. Schmidlein. 2009. Mapping continuous fields of forest alpha and beta diversity. *Applied Vegetation Science* 12:429–439.
- Feilhauer, H., U. Faude, and S. Schmidlein. 2011. Combining Isomap ordination and imaging spectroscopy to map continuous floristic gradients in a heterogeneous landscape. *Remote Sensing of Environment* 115:2513–2524.
- Ferrier, S., and A. Guisan. 2006. Spatial modelling of biodiversity at the community level. *Journal of Applied Ecology* 43: 393–404.
- Filella, I., and J. Penuelas. 1994. The red edge position and shape as indicators of plant chlorophyll content, biomass and hydric status. *International Journal of Remote Sensing* 15: 1459–1470.
- Foster, J., and P. Townsend. 2004. Linking hyperspectral imagery and forest inventories for forest assessment in the central Appalachians. Pages 76–86 in *Proceedings of the 14th Central Hardwood Forest Conference*, 16–19 March, Wooster, Ohio, U.S. Department of Agriculture, Forest Service, Northeastern Research Station, Wooster.
- Gergely, K. J., and A. McKerrow. 2016. Terrestrial ecosystems—National inventory of vegetation and land use (version 1.1, August 2016): U.S. Geological Survey Fact Sheet 2013–3085 1 p. <https://pubs.usgs.gov/fs/2013/3085/>
- Ghiyam, A., and H. Z. M. Shafri. 2008. A review on hyperspectral remote sensing for homogeneous and heterogeneous forest biodiversity assessment. *International Journal of Remote Sensing* 31:1837–1856.
- Gitelson, A. A., M. N. Merzlyak, and O. B. Chivkunova. 2001. Optical properties and nondestructive estimation of anthocyanin content in plant leaves. *Photochemistry and Photobiology* 74:38.

- Gitelson, A. A., Y. Zur, O. B. Chivkunova, and M. N. Merzlyak. 2002. Assessing carotenoid content in plant leaves with reflectance spectroscopy. *Photochemistry and Photobiology* 75:272–281.
- Goslee, S. C., and D. L. Urban. 2007. The ecodist package for dissimilarity-based analysis of ecological data. *Journal of Statistical Software* 22:1–19.
- Gu, H., A. Singh, and P. A. Townsend. 2015. Detection of gradients of forest composition in an urban area using imaging spectroscopy. *Remote Sensing of Environment* 167:168–180.
- Haboudane, D., J. R. Miller, E. Pattey, P. J. Zarco-Tejada, and I. B. Strachan. 2004. Hyperspectral vegetation indices and novel algorithms for predicting green LAI of crop canopies: Modeling and validation in the context of precision agriculture. *Remote Sensing of Environment* 90:337–352.
- Hakkenberg, C. R., D. D. Tarasi, and R. K. Peet. 2017. Community/continuum in biogeography. Pages 1–4 in D. Richardson, N. Castree, M. F. Goodchild, A. L. Kobayashi, W. Liu, and R. A. Marston, editors. *International encyclopedia of geography: people, the earth, environment, and technology*. John Wiley & Sons, Ltd., Hoboken, New Jersey, USA.
- Higgins, M. A., G. P. Asner, R. E. Martin, D. E. Knapp, C. Anderson, T. Kennedy-Bowdoin, R. Saenz, A. Aguilar, and S. Joseph Wright. 2014. Linking imaging spectroscopy and LiDAR with floristic composition and forest structure in Panama. *Remote Sensing of Environment* 154:358–367.
- Hill, R., and A. Thomson. 2005. Mapping woodland species composition and structure using airborne spectral and LiDAR data. *International Journal of Remote Sensing* 26:3763–3779.
- Houlahan, J. E., S. T. McKinney, T. M. Anderson, and B. J. McGill. 2016. The priority of prediction in ecological understanding. *Oikos* 126:1–7.
- Jennings, M. D., D. Faber-Langendoen, O. L. Loucks, R. K. Peet, and D. Roberts. 2009. Standards for associations and alliances of the US. *National standards classification vegetation*. *Ecological Monographs* 79:173–199.
- Kampe, T., B. R. Johnson, M. Kuester, and M. Keller. 2010. NEON: the first continental-scale ecological observatory with airborne remote sensing of vegetation canopy biochemistry and structure. *Journal of Applied Remote Sensing* 4:1–24.
- Kane, V. R., R. J. McGaughey, J. D. Bakker, R. F. Gersonde, J. A. Lutz, and J. F. Franklin. 2010. Comparisons between field- and LiDAR-based measures of stand structural complexity. *Canadian Journal of Forest Research* 40:761–773.
- Kaufman, L., and P. J. Rousseeuw. 2005. *Finding groups in data: an introduction to cluster analysis* (Wiley series in probability and statistics). John Wiley & Sons, Hoboken, New Jersey, USA.
- Kohavi, R. 1995. A study of cross-validation and bootstrap for accuracy estimation and model selection. *Ijcai* 14:1137–1145.
- Kokaly, R. F., D. G. Despain, R. N. Clark, and K. E. Livo. 2003. Mapping vegetation in Yellowstone National Park using spectral feature analysis of AVIRIS data. *Remote Sensing of Environment* 84:437–456.
- Kruskal, J. B. 1964. Nonmetric multidimensional scaling: A numerical method. *Psychometrika* 29:115–129.
- Legendre, P., and L. Legendre. 2012. *Numerical ecology*. Third English edition. Elsevier, Amsterdam, The Netherlands.
- Leutner, B. F., B. Reineking, J. Müller, M. Bachmann, C. Beierkuhnlein, S. Dech, and M. Wegmann. 2012. Modeling forest α -diversity and floristic composition – on the added value of LiDAR plus hyperspectral remote sensing. *Remote Sensing* 4:2818–2845.
- Liaw, A., and M. Wiener. 2002. Classification and regression by random forest. *R News* 2:18–22.
- Martin, M., S. Newman, J. Aber, and R. Congalton. 1998. Determining forest species composition using high spectral resolution remote sensing data. *Remote Sensing of Environment* 65:249–254.
- Matthews, E. R., R. K. Peet, and A. S. Weakley. 2011. Classification and description of alluvial plant communities of the Piedmont region, North Carolina, USA. *Applied Vegetation Science* 14:485–505.
- McGill, B. J., B. J. Enquist, E. Weiher, and M. Westoby. 2006. Rebuilding community ecology from functional traits. *Trends in Ecology and Evolution* 21:178–185.
- Middleton, M., P. Narhi, H. Arkimaa, E. Hyvonen, V. Kuosmanen, P. Treitz, and R. Sutinen. 2012. Ordination and hyperspectral remote sensing approach to classify peatland biotopes along soil moisture and fertility gradients. *Remote Sensing of Environment* 124:596–609.
- Naidoo, L., M. A. Cho, R. Mathieu, and G. Asner. 2012. Classification of savanna tree species, in the Greater Kruger National Park region, by integrating hyperspectral and LiDAR data in a random forest data mining environment. *ISPRS Journal of Photogrammetry and Remote Sensing* 69:167–179.
- Neumann, C., G. Weiss, S. Schmidtlein, S. Itzerott, A. Lausch, D. Doktor, and M. Brell. 2015. Gradient-based assessment of habitat quality for spectral ecosystem monitoring. *Remote Sensing* 7:2871–2898.
- Ohmann, J. L., and M. J. Gregory. 2002. Predictive mapping of forest composition and structure with direct gradient analysis and nearest-neighbor imputation in coastal Oregon, U.S.A. *Canadian Journal of Forest Research* 32:725–741.
- Okin, G. S., D. A. Roberts, B. Murray, and W. J. Okin. 2001. Practical limits on hyperspectral vegetation discrimination in arid and semiarid environments. *Remote Sensing of Environment* 77:212–225.
- Pal, M. 2005. Random forest classifier for remote sensing classification. *International Journal of Remote Sensing* 26:217–222.
- Peet, R. K., and N. L. Christensen. 1988. Changes in species diversity during secondary forest succession on the North Carolina piedmont. Pages 233–245 in J. J. Dunning, M. J. A. Werger, and J. H. Willems, editors. *Diversity and pattern in plant communities*. SPB Academic Publishing, The Hague, The Netherlands.
- Peet, R. K., and D. W. Roberts. 2013. Classification of natural and semi-natural vegetation. Pages 28–70 in E. van der Maarel and J. Franklin, editors. *Vegetation ecology*. Second edition. John Wiley & Sons, Oxford, UK.
- Peet, R., T. Wentworth, and P. White. 1998. A flexible, multi-purpose method for recording vegetation composition and structure. *Castanea* 63:262–274.
- Peet, R., M. Lee, M. Jennings, and D. Faber-Langendoen. 2012. VegBank – a permanent, open-access archive for vegetation-plot data. *Biodiversity and Ecology* 4:233–241.
- Prasad, A. M., L. R. Iverson, and A. Liaw. 2006. Newer classification and regression tree techniques: bagging and random forests for ecological prediction. *Ecosystems* 9:181–199.
- Price, J. C. 1994. How unique are spectral signatures? *Remote Sensing of Environment* 49:181–186.
- R Core Team. 2016. *R: A language and environment for statistical computing*. R Foundation for Statistical Computing, Vienna, Austria. www.r-project.org
- Roberts, D. W. 2015. Vegetation classification by two new iterative reallocation optimization algorithms. *Plant Ecology* 216:741–758.
- Roberts, D. W. 2016a. *labdsv: ordination and multivariate analysis for ecology*. R package version 1.8-0. <https://CRAN.R-project.org/package=labdsv>

- Roberts, D. W. 2016b. *optpart*: optimal partitioning of similarity relations. R package version 2.2-0. <https://CRAN.R-project.org/package=optpart>
- Rocchini, D., J. L. Hernández-Stefanoni, and K. S. He. 2015. Advancing species diversity estimate by remotely sensed proxies: A conceptual review. *Ecological Informatics* 25:22–28.
- Roth, K. L., D. A. Roberts, P. E. Dennison, M. Alonzo, S. H. Peterson, and M. Beland. 2015. Differentiating plant species within and across diverse ecosystems with imaging spectroscopy. *Remote Sensing of Environment* 167:135–151.
- Running, S. W., and J. C. Coughlan. 1988. A general model of forest ecosystem processes for regional applications. *Ecological Modelling* 42:125–154.
- Schmidtlein, S., and J. Sassin. 2004. Mapping of continuous floristic gradients in grasslands using hyperspectral imagery. *Remote Sensing of Environment* 92:126–138.
- Schmidtlein, S., P. Zimmermann, R. Schupferling, and C. Weiss. 2007. Mapping the floristic continuum: Ordination space position estimated from imaging spectroscopy. *Journal of Vegetation Science* 18:131–140.
- Singh, A., S. P. Serbin, B. E. McNeil, C. C. Kingdon, and P. A. Townsend. 2015. Imaging spectroscopy algorithms for mapping canopy foliar chemical and morphological traits and their uncertainties. *Ecological Applications* 25:2180–2197.
- Stone, J. R., J. W. Gilliam, D. K. Cassel, R. B. Daniels, L. A. Nelson, and H. J. Kleiss. 1985. Effect of erosion and landscape position on the productivity of Piedmont soils. *Soil Science Society of America Journal* 49:987–991.
- Thenkabail, P. S., E. A. Enclona, M. S. Ashton, and B. Van Der Meer. 2004. Accuracy assessments of hyperspectral waveband performance for vegetation analysis applications. *Remote Sensing of Environment* 91:354–376.
- Thessler, S., K. Ruokolainen, H. Tuomisto, and E. Tomppo. 2005. Mapping gradual landscape-scale floristic changes in Amazonian primary rain forests by combining ordination and remote sensing. *Global Ecology and Biogeography* 14:315–325.
- Tilman, D., J. M. H. Knops, D. Wedin, P. B. Reich, and E. Siemann. 1997. The influence of functional diversity and composition on ecosystem processes. *Science* 277:1300–1302.
- Tološi, L., and T. Lengauer. 2011. Classification with correlated features: Unreliability of feature ranking and solutions. *Bioinformatics* 27:1986–1994.
- Torabzadeh, H., F. Morsdorf, and M. E. Schaepman. 2014. Fusion of imaging spectroscopy and airborne laser scanning data for characterization of forest ecosystems – A review. *ISPRS Journal of Photogrammetry and Remote Sensing* 97:25–35.
- Ustin, S. L., and J. A. Gamon. 2010. Remote sensing of plant functional types. *New Phytologist* 186:795–816.
- van Ewijk, K. Y., C. F. Randin, P. M. Treitz, and N. A. Scott. 2014. Predicting fine-scale tree species abundance patterns using biotic variables derived from LiDAR and high spatial resolution imagery. *Remote Sensing of Environment* 150:120–131.
- Weakley, A. S. 2015. *Flora of the Southern and Mid-Atlantic States*. Working draft of 21 May 2015. University of North Carolina Herbarium (NCU), Chapel Hill, North Carolina, USA.
- Whittaker, R. H. 1967. Gradient analysis of vegetation. *Biological Reviews* 42:207–264.
- Zhang, G., and Y. Lu. 2012. Bias-corrected random forests in regression. *Journal of Applied Statistics* 39:151–160.

SUPPORTING INFORMATION

Additional supporting information may be found online at: <http://onlinelibrary.wiley.com/doi/10.1002/eap.1638/full>

DATA AVAILABILITY

Data available from the VegBank Data Repository: <http://vegbank.org/cite/VB.pj.11067.DUKEBLACKWOODNA>